RSC Advances

PAPER

View Article Online
View Journal | View Issue

Cite this: *RSC Adv.*, 2022, **12**, 11128

Ti_3C_2 nanosheets with broad-spectrum antioxidant activity for cytoprotection against oxidative stress†

Hongqi Geng,[ab] Yaping Ren,[b] Gang Qin,[a] Tao Wen, *[c] Quan Liu,[b] Haiyan Xu [c] and Weiwei He *[b]

Redox regulation in biological systems represents a fascinating method for treatment and prevention of oxidative stress induced diseases. The key and difficult point is to find ideal materials with excellent antioxidant capability and good biocompatibility. To this end, ultra-thin two-dimensional MXene (Ti_3C_2) nanosheets (NSs) were investigated for their antioxidant capability. It is found that Ti_3C_2 NSs can scavenge efficiently reactive oxygen and nitrogen species ($^{\bullet}OH$, H_2O_2, $O_2^{\bullet-}$ and $^{\bullet}NO$), $ABTS^{+\bullet}$ and $DPPH^{\bullet}$ free radicals in a concentration dependent manner, showing broad-spectrum antioxidant activities. Ti_3C_2 NSs exhibit higher antioxidant activity and broader antioxidant capability than natural antioxidant molecules. The significant role of PEG modified Ti_3C_2 with good stability in preventing cell damage against oxidative stress was demonstrated. Upon treatment of H_2O_2 induced oxidative stress with Ti_3C_2, the intracellular ROS level decreases and the cell survival rate increases significantly. An antioxidant mechanism based on gradient oxidation was proposed to account for the superior antioxidant activity of Ti_3C_2. Our result proves that ultra-thin MXenes as antioxidants have great potential in preventing oxidative stress caused biological damage.

Received 23rd February 2022
Accepted 5th April 2022

DOI: 10.1039/d2ra01225a

rsc.li/rsc-advances

1. Introduction

Oxidative stress is a state of imbalance between oxidation and antioxidation in biological systems, and is considered to be one of the critical factors leading to aging and many intractable diseases.[1–3] Reactive oxygen species (ROS) and reactive nitrogen species (RNS), including superoxide ($O_2^{\bullet-}$), hydrogen peroxide (H_2O_2), hydroxyl radicals ($^{\bullet}OH$), $^{\bullet}NO$ and $ONOO^-$, play important roles in cellular life cycles.[4] Unfortunately, the overproduction of ROS and RNS has been recognized as the direct cause of damage to cellular components (cell membranes, protein structures, and DNA) and their functions.[5] Redox regulation represents a fascinating way to relieve oxidative stress. The key point is to find suitable materials with excellent antioxidant capability and low toxicity.

There are effective ways to alleviate oxidative stress through antioxidant small molecule, enzymes and enzyme-like nanomaterials. A number of literatures based on *in vitro* and *in vivo* experiments provide evidences that antioxidant molecules represent a rational curative strategy to reduce ROS/RNS as well as prevent and cure oxidative stress induced diseases.[6,7] Natural antioxidants suffer from their low antioxidant efficiency, and sometimes their oxidation can yield unfriendly products. Natural enzymes signify an important role in defense oxidative stress, but the "paradoxical" roles of antioxidant enzymes triggering metabolic disorders also was revealed.[8] In addition, the enzymes work only to catalyze the reduction of specific oxidative species, such as superoxide dismutase (SOD) and catalase. Enzymelike nanomaterials have been named as nanozymes because of their intrinsic activity to mimic natural enzymes.[9–12] Most reported nanozymes belong to the oxidoreductases family and show great potential in regulating ROS level.[13–20] In addition, nanozymes (*e.g.* Pt based and metal oxide) often function to mimic multiple redox enzymes (oxidase, SOD, peroxidase and catalase).[21–25] Such multiple enzymelike activity enables nanozymes with antioxidant activity while also having pro-oxidative functions. Therefore, it is highly required to develop ideal antioxidant nanomaterial with high efficiency and broad spectrum for biomedical study and clinical applications.

MXenes have been found as a family of two-dimensional (2D) metal carbides and nitrides, which show tunable electronic, optical and catalytic properties.[26–30] Because of good biocompatibility and low cytotoxicity, MXenes have been explored for biomedical applications, *e.g.* antibacterial, cancer therapeutics and diagnosis.[31–33] Especially, few or monolayer MXenes are very sensitive to be oxidized because of abundant low-valence metal spices, and can be used as antioxidant to defense the oxidative damage.[34] Recently, V_2C, Ti_3C_2 and Nb_2C MXenes have been

[a]School of Materials Science and Engineering, Henan Polytechnic University, Jiaozuo, Henan 454000, P. R. China. E-mail: heweiweixcu@gmail.com

[b]Key Laboratory of Micro-Nano Materials for Energy Storage and Conversion of Henan Province, College of Chemical and Materials Engineering, Institute of Surface Micro and Nano Materials, Xuchang University, Xuchang, Henan 461000, P. R. China

[c]Institute of Basic Medical Sciences Chinese Academy of Medical Sciences, School of Basic Medicine Peking Union Medical College, Beijing 100005, P. R. China. E-mail: went@ibms.pumc.edu.cn

† Electronic supplementary information (ESI) available: Fig. S1–S9 and Tables S1, S2. See https://doi.org/10.1039/d2ra01225a

reported to exhibit ROS scavenging activity and show potential in alleviation of ROS induced neurons and acute kidney injury.[35–40] But we still know very little about their antioxidant behavior, for example, the antioxidant mechanism and the antioxidant capability toward various active species and free radicals. To fully understand the antioxidant capability and mechanism of Ti_3C_2 for better applications, we systematically evaluate their antioxidant capability toward ROS, RNS and free radicals as well as demonstrate the potential in preventing oxidative stress induced cell damage. The primary objective of this study is to investigate the high-efficiency and broad-spectrum antioxidant activity of Ti_3C_2 nanosheets and understand their antioxidant mechanism.

2. Experimental

2.1 Chemical and materials

Ti_3AlC_2 MAX powder (400 mesh) was purchased from 11 Technology, China. Hydrofluoric acid (HF), hydrogen peroxide (H_2O_2), horseradish peroxidase (HRP) and xanthine oxidase (XOD) were purchased from Sinopharm Chemical Reagent Co., Ltd (Beijing, China) and 2,2′-azinobis-(3-ethylbenzthiazoline-6-sulphonate) (ABTS), (*S*)-nitroso-*N*-acetylpenicillamine (SNAP), and ferrous sulfate ($FeSO_4$) were commercially available from Aladdin Industrial Co. (CA, USA). 1,1-Diphenyl-2-picrylhydrazyl radical 2,2-diphenyl-1-(2,4,6-trinitrophenyl)hydrazyl (DPPH) was purified from Shanghai Macklin Biochemical Co., Ltd. Tetramethyl ammonium hydroxide (TMAOH), diethylenetriaminepentaacetic acid (DTPA) and xanthine were purchased from Sigma-Aldrich (Shanghai, China). 5,5-Dimethyl-1-pyrroline-*N*-oxide (DMPO) and 5-*tert*-butoxycarbonyl-5-methyl-1-pyrroline-*N*-oxide (BMPO) were purchased from Tongren Institute of Chemistry. 2-Phenyl-4,4,5,5-tetramethylimidazoline-*q*-oxyl 3-oxide (PTIO) was obtained from Shanghai Maokang Biotechnology Co., Ltd. Milli-Q water (18 MΩ cm) was used in the preparation of all solutions.

2.2 Characterization

UV-Vis absorption spectra were obtained using a Cary 5000 UV-Vis spectrometer (Varian, USA) and a matched quartz cuvette with a path length of 1 cm. The crystal structures of the Ti_3C_2 NSs were characterized by X-ray diffraction (XRD, D8 Advance diffractometer, Bruker, Germany) using monochromatized Cu Kα radiation ($\lambda = 1.5418$ Å). Transmission electron microscope (TEM) and high resolution TEM (HRTEM) images were captured on a Tecnai G2 F20 U-Twin electron microscope with an accelerating voltage of 200 kV. X-ray photoelectron spectroscopy (XPS) was performed with a Thermo ESCALAB 250XI multifunctional imaging electron spectrometer (Thermo Fisher Scientific, USA) using 150 W Al K_α radiation and a base pressure of approximately 3×10^{-9} mbar. The binding energies were calibrated to the C 1s line at 284.8 eV. Raman spectra was performed with a Renishaw Raman microscope (inVia, Renishaw, UK) using an excitation laser with 532 nm wavelength. AFM images were tested by Dimension Icon produced by Bruker Germany and zeta potential was tested using Malvern Zetasizer Nano ZS90. Electron spin-resonance (ESR) spectra were obtained using an EMX micro electron paramagnetic resonance spectrometer (Bruker, Germany). The measurements were carried out at room temperature under the following conditions: microwave power 2 mW, modulation amplitude 1.0 G, attenuation 30 dB, and scan range of 100 G.

2.3 Synthesis of multilayer Ti_3C_2

10 mL 50 wt% HF was added to a 25 mL Teflon tank, and 1 g Ti_3AlC_2 was added to the solution gradually and carefully due to the exothermic reaction between Ti_3AlC_2 and HF solution. The reaction between Ti_3AlC_2 and HF follows the eqn (1)–(3).[26]

$$Ti_3AlC_2 + 3HF = AlF_3 + 3/2H_2 + Ti_3C_2 \quad (1)$$

$$Ti_3C_2 + 2H_2O = Ti_3C_2(OH)_2 + H_2 \quad (2)$$

$$Ti_3C_2 + 2HF = Ti_3C_2F_2 + H_2 \quad (3)$$

After stirring at room temperature for 24 h, the solution was centrifuged at 3500 rpm for 10 min until the pH > 6. The products were dried under vacuum at 80 °C for 24 h. HF is very dangerous, it should be extremely careful during operation.

2.4 Synthesis of 2D Ti_3C_2 nanosheets

0.2 g multilayer Ti_3C_2 powder was dispersed in 60 mL aqueous solution of 2 wt% TMAOH for 30 min, and 0.352 g AA was added. After mixing, the resulting mixture was transferred to a 100 mL Teflon stainless steel autoclave, sealed and placed in oven at 140 °C for 24 h.[41] Then, the TMAOH solution and AA were removed by centrifugation at 10 000 rpm for three times. The black precipitate was resuspended into 60 mL deionized water and transferred to a conical flask, and ultrasonic was performed in argon atmosphere for 2 h. Then, a colloidal solution of 2D Ti_3C_2 nanosheets was collected by centrifugation for 20 min at 8000 rpm. The 2D Ti_3C_2 nanosheets were collected *via* drying in a vacuum freeze dryer for at least 24 h. The resulting powder was dispersed to 1 mg mL^{-1} in deionized water.

2.5 Synthesis of Ti_3C_2–PEG

In order to completely coat the Ti_3C_2 surface with PEG molecules, an excessive amount of PEG was used with a PEG/Ti_3C_2 mass ratio of 20 : 1. 0.1 g of PEG-6000 were dispersed into 5 mL water and mixed with 5 mL Ti_3C_2 nanosheets solution (1 mg mL^{-1}). The aqueous solution was kept stirring overnight. The product was centrifuged three times at 13 000 rpm for 30 min to remove excess PEG molecules. The collected black precipitate was freeze-dried, dispersed to 0.5 mg mL^{-1} in deionized water.

2.6 Synthesis of Ti_3C_2-A and Ti_3C_2-B (the Ti_3C_2 nanosheets after oxidation by $ABTS^{+\bullet}$ and H_2O_2)

2 mL freshly made Ti_3C_2 (1 mg mL^{-1}) was stirred with excess 2,2′-azinobis-(3-ethylbenzthiazoline-6-sulphonate) free radicals ($ABTS^{+\bullet}$) overnight. Then, the precipitation was collected by centrifugation three times at 8000 rpm for 10 min. 4 mL deionized water was added into the precipitation to prepare

Ti_3C_2-A with a final concentration of 0.5 mg mL^{-1}. Following the similar procedure, Ti_3C_2-B (Ti_3C_2 reacting with H_2O_2) with concentration of 0.5 mg mL^{-1} was prepared by stirring, centrifugation and constant volume.

2.7 Measurement of radical scavenging activity of Ti_3C_2 NSs

2.7.1 $ABTS^{+\cdot}$ and DPPH$^{\cdot}$ scavenging activity. ABTS and DPPH assays are used to measure the total antioxidant capacity of Ti_3C_2 and Ti_3C_2–PEG NSs. 0.0374 g ABTS powders was dissolved into 30 mL deionized water, followed by addition of 0.0066 g $K_2S_2O_8$ under stirring and dark reaction for 12 h. To test the $ABTS^{+\cdot}$ reduction, 0.5 mg mL^{-1} Ti_3C_2 or Ti_3C_2–PEG with varied volume (3, 5, 7, 10, 15 μL) is added into 3 mL $ABTS^{+\cdot}$ solution (O.D. = ~1.2). To test the DPPH$^{\cdot}$ reduction, 2.5 mL of 1 mg mL^{-1} DPPH$^{\cdot}$ ethanol solution was added with 0.5 mL of deionized water. Then, 0.5 mg mL^{-1} Ti_3C_2 or Ti_3C_2–PEG with different volumes of (3, 5, 7, 10, 15 μL) were added. Two minutes later, the UV-Vis spectra were recorded to measure the reduction of $ABTS^{+\cdot}$ and DPPH$^{\cdot}$.

2.7.2 H_2O_2 scavenging activity. The H_2O_2 scavenging ability of Ti_3C_2 was analyzed by HRP–H_2O_2–TMB system. 20 μL H_2O_2 (0.1 M) is firstly mixed with Ti_3C_2 and Ti_3C_2–PEG with desirable concentrations in 3 mL H_2O, 2 min later, 20 μL TMB (20 mM) and 10 μL HRP (1 μg mL^{-1}) were added into the above mixture to initiate the TMB oxidation. After 3 min of reaction, the absorption spectra showing characteristic absorption at 652 nm was recorded by UV-Vis spectrometer.

2.7.3 $^{\cdot}OH$ scavenging activity. The $^{\cdot}OH$ was generated by classic Fenton reaction between Fe^{2+} and H_2O_2, and the production of $^{\cdot}OH$ is monitored by both UV-Vis spectra and ESR. For UV-Vis spectra test, 20 μL TMB (20 mM), 20 μL H_2O_2 (0.1 M) and 20 μL $FeSO_4$ (2 mM) were mixed in 3 mL H_2O, then (3, 5, 7, 10, 15 μL) 0.5 mg mL^{-1} Ti_3C_2 and Ti_3C_2–PEG solution was added. For ESR test, 10 mM H_2O_2 was mixed with 50 mM DMPO and 10 mM Fe^{2+} in the absence and presence of Ti_3C_2 with different concentrations or antioxidant agents. At selected time intervals, the UV-Vis spectra and ESR spectra was recorded.

2.7.4 SOD-like activity. ESR was used to test SOD-like activity to scavenge superoxide of Ti_3C_2 and Ti_3C_2–PEG. Typically, 10 μL xanthine (5 mM) is mixed with 10 μL DTPA (0.25 mM), 5 μL BMPO (250 mM) and Ti_3C_2 or Ti_3C_2–PEG with different concentrations, then 5 μL XOD (0.4 U mL^{-1}) was added to initiate the production of superoxide anion. The SOD-like enzyme activity of antioxidant was analyzed by BMPO/$^{\cdot}OOH$ signal changes.

2.7.5 $^{\cdot}NO$ scavenging activity. The $^{\cdot}NO$ scavenging activity of Ti_3C_2 was tested by ESR. $^{\cdot}NO$ was produced SNAP and was trapped by PTIO$^{\cdot}$ to form typical ESR signals. For the ESR measurement, 10 μL SNAP (2 mM) was mixed with 10 μL PTIO$^{\cdot}$ (2 μM) in PBS solution in the absence and presence of Ti_3C_2 or Ti_3C_2–PEG or antioxidant molecule.

2.8 Cell culture

Mouse fibroblast cell line NIH3T3 was purchased from the Cell Center of Institute of Basic Medical Sciences, Chinese Academy of Medical Sciences & Peking Union Medical College (Beijing, China). NIH3T3 was cultured in high-glucose basal Dulbecco's modified Eagle's medium (DMEM) (Hyclone) containing 10% fetal bovine serum (FBS) (Invitrogen), 4500 mg L^{-1} glucose, 4 mM L-glutamine, and 0.1% streptomycin and penicillin G at 37 °C with 5% CO_2.

2.9 Cell viability assay

NIH3T3 were seeded into 96-well cell culture plates at a density of 1×10^4 cells per well and cultured 24 h for adherence. The cells were incubated with 100 μL DMEM containing different concentration of Ti_3C_2–PEG or/and 25 μM H_2O_2 at 37 °C for 24 h, followed by washing with PBS. Photograph were acquired using an EVOS M7000 imaging system (Thermo Scientific). After the cells incubated with 110 μL fresh medium containing 10 μL Cell Counting Kit-8 (CCK-8, Dojindo Molecular Technologies, Inc.) for about 2 h, the absorbance of the medium was measured at 450 nm using the Varioskan LUX multimode microplate reader (Thermo Scientific). The measurements were carried out in three parallel lines, and the relative cell viability was expressed as a percentage of the control.

2.10 Intracellular ROS measurement

NIH3T3 were seeded at a density of 1×10^5 cells per well in the 24-well cell culture plate and kept overnight to adhere. The cells were treated with 25 μM H_2O_2 in the absent and present of 5 μg mL^{-1} Ti_3C_2–PEG for 24 h at 37 °C and then washed with PBS. After that, PBS containing 10 μM DCFH-DA (Sigma-Aldrich, USA) was added at 37 °C for 30 min and then washed with PBS twice. Photograph was acquired using an EVOS M7000 imaging system. Finally, the cells were detached from the plates with trypsin, and collected by centrifugation. Flow cytometric analysis was conducted on all the groups, using an excitation wavelength of 488 nm and emission wavelength of 525 nm (AccuriTM C6 flow cytometer, BD Biosciences, San Jose, CA). All groups had three replicate wells.

2.11 Statistical analysis

The data are shown as mean ± standard deviation (SD) for all treatment groups. Statistical significance was ascertained through one way ANOVA with SPSS software (SPSS17.0).

3. Results and discussion

3.1 Fabrication and characterization of Ti_3C_2 NSs

Few-layered Ti_3C_2 MXene nanosheets (NSs) were synthesized by a typical exfoliation and intercalation process (Fig. 1a).[41,42] The tight "sandwich" structure of the Ti_3AlC_2 MAX-phase was confirmed by SEM image (Fig. 1b). Multiple-layered Ti_3C_2 with accordion structure were obtained *via* selective etching of Al layer by using HF solution (Fig. 1c). Then, few-layered Ti_3C_2 nanosheets were formed by further TMAOH intercalation, hydrothermal and ultrasonic treatment under anti-oxidation protection. The as-prepared Ti_3C_2 nanosheets are well dispersed in aqueous solution due to abundant hydrophilic groups on surface. TEM image shows the few-layer structure of Ti_3C_2 NSs with a lateral dimension of about 200 nm (Fig. 1d).

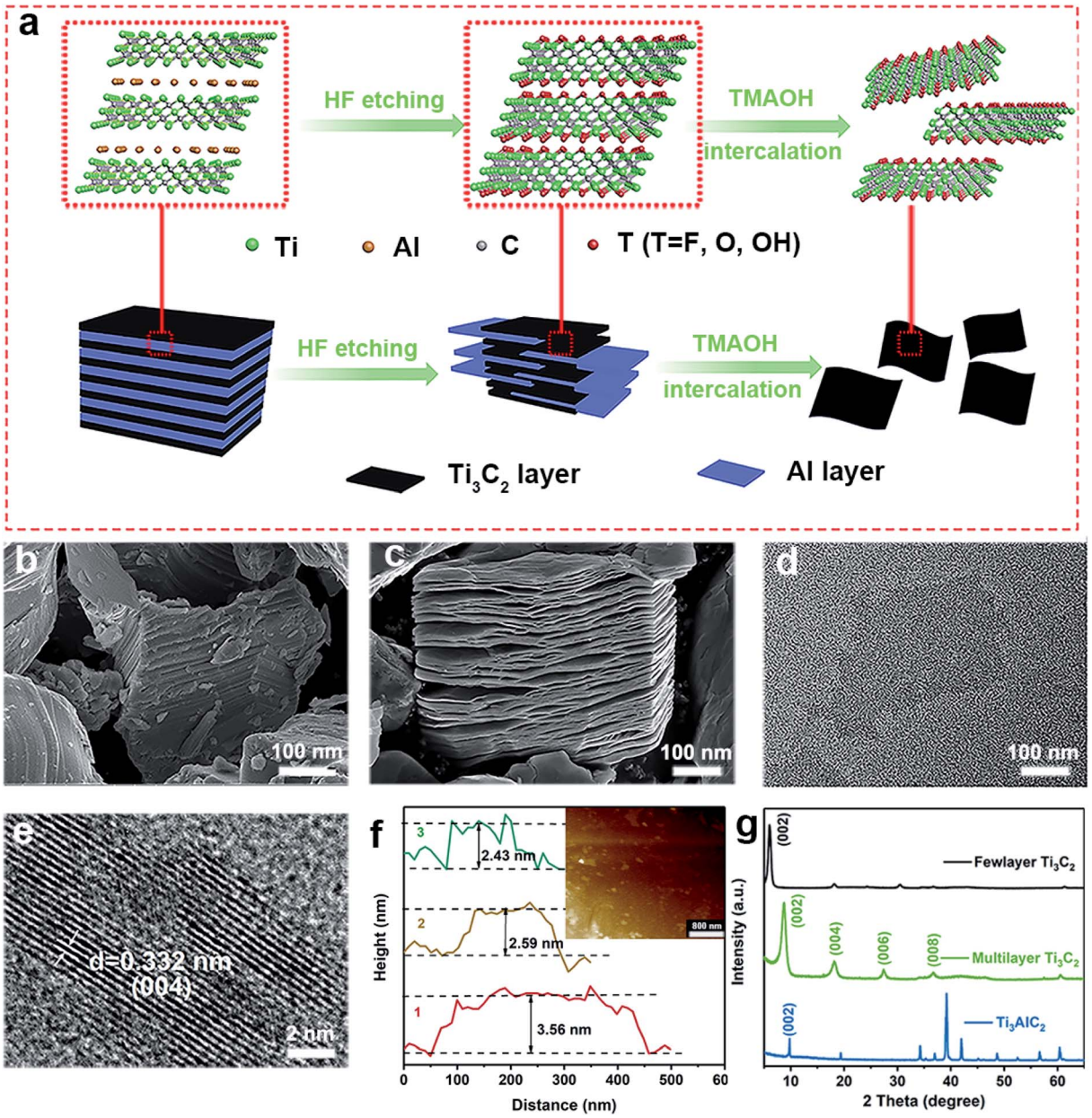

Fig. 1 Fabrication and characterization of Ti_3C_2 MXene NSs. (a) Schematic diagram for the procedure to prepare few layered Ti_3C_2 NSs, insets illustrate the corresponding chemical structures. SEM image of (b) Ti_3AlC_2 and (c) multilayer Ti_3C_2, TEM (d), HRTEM (e) and AFM (f) image of Ti_3C_2 NSs, (g) XRD patterns of Ti_3AlC_2, multilayer Ti_3C_2 and few layered Ti_3C_2 nanosheets.

HRTEM image shows the well-defined lattice planes of selected region (Fig. 1e), and the lattice spacing is calculated to be 0.332 nm, corresponding to the interplanar distance of (004) plane. The averaged thickness of Ti_3C_2 NSs is ~2.59 nm, denoting that the synthesized Ti_3C_2 is composed of two or three layers (Fig. 1f). XRD pattern shows that after HF etching, the diffraction peak of Ti_3AlC_2 at 39° disappeared, while the characteristic peak of Ti_3C_2 at 8.8° appeared (Fig. 1g). This indicates that Al intercalation is etched away and Ti_3AlC_2 is completely converted to multilayer Ti_3C_2. With further stripping, the characteristic peak (002) of multilayer Ti_3C_2 shifts to 6.4°, finally forming the Ti_3C_2 NSs.[26,41,43]

3.2 Antioxidant activity of Ti_3C_2 NSs by scavenging free radicals, ROS and RNS

The antioxidant efficiency is determined by the category and degree of removing oxidative free radicals. $ABTS^{+\bullet}$ radicals is an oxidative product of ABTS.[44] $DPPH^{\bullet}$ is a well-known stable free radical containing unpaired electrons, it has a strong absorption band in the visible region at 517 nm owing to its odd electron, which disappears when this electron is paired up or forms a H-bond in the presence of antioxidants.[45] $ABTS^{+\bullet}$ and $DPPH^{\bullet}$ are two standard assays commonly used to evaluate the total antioxidant capabilities of natural antioxidants. The reduction of $ABTS^{+\bullet}$ is dominated by the electron transfer

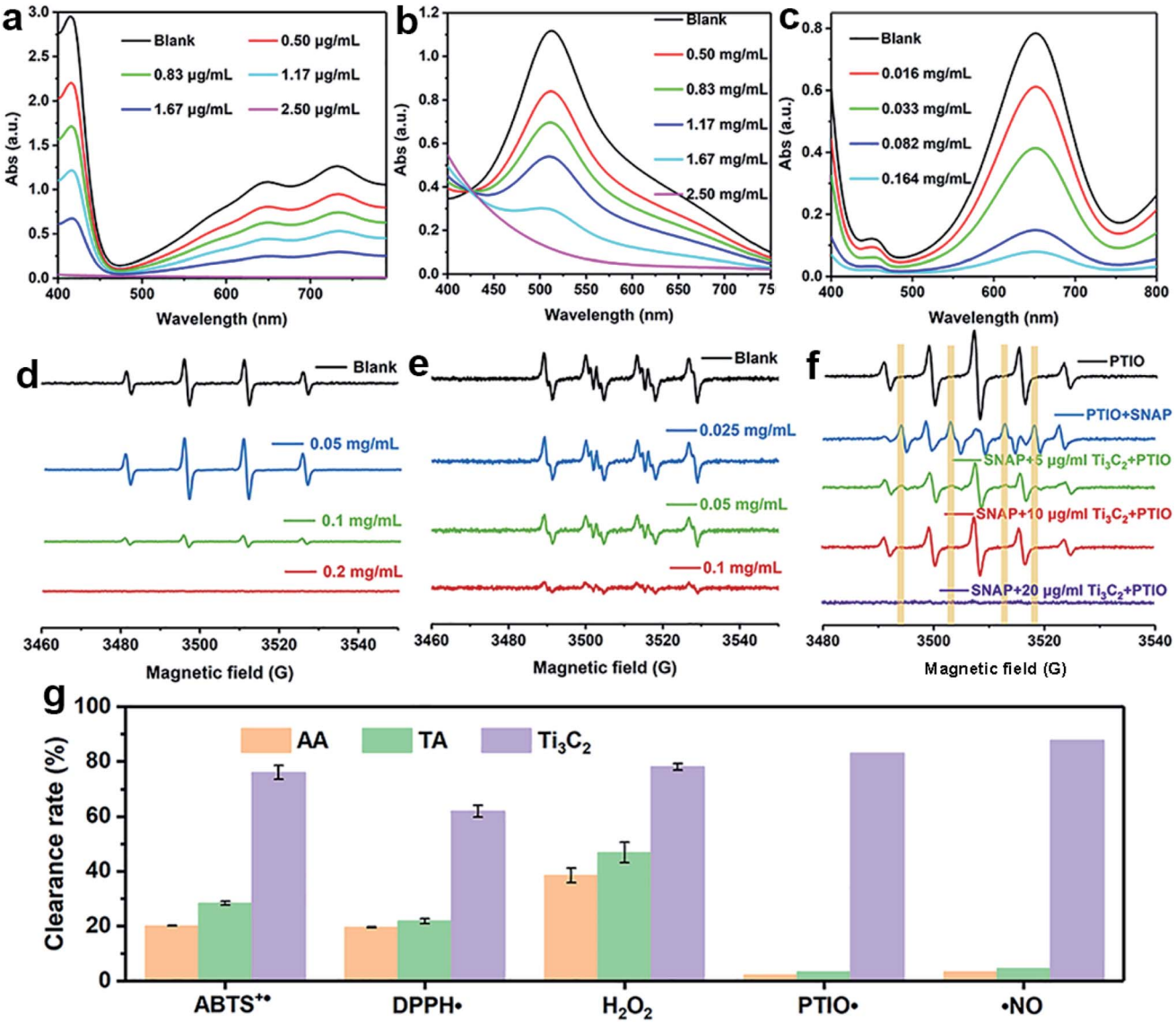

Fig. 2 Antioxidant activity of Ti_3C_2. $ABTS^{+\bullet}$ and DPPH$^\bullet$ scavenging activity: UV-Vis spectra of $ABTS^{+\bullet}$ (a) and DPPH$^\bullet$ solutions (b) in different concentration of Ti_3C_2 NSs, H_2O_2 scavenging activity (c) UV-Vis spectra of samples containing TMB, HRP and H_2O_2 in different concentration of Ti_3C_2 NSs, (d) ESR spectra of BMPO/$^\bullet$OH generated from the samples containing H_2O_2, BMPO, Fe^{2+} and with different concentration of Ti_3C_2, (e) ESR spectra of BMPO/$^\bullet$OOH generated from samples containing xanthine, XOD, BMPO and different concentration of Ti_3C_2, (f) ESR spectra of the PTIO$^\bullet$ solution alone and the PTIO$^\bullet$ solutions with $^\bullet$NO-generator SNAP in the absence or presence of different concentration of Ti_3C_2, (g) comparison of Ti_3C_2 with TA and AA in scavenging free radicals, ROS and RNS.

process, while the reduction of DPPH$^\bullet$ mainly involves the proton transfer process.[46,47] Both $ABTS^{+\bullet}$ and DPPH$^\bullet$ solution show typical color and characteristic absorption band at visible region, this provides a convenient way to compare the antioxidant activity of Ti_3C_2 nanosheets by monitoring the change in absorbance. It shows clearly that the addition of Ti_3C_2 can efficiently reduce $ABTS^{+\bullet}$ and DPPH$^\bullet$ free radicals (Fig. 2a and b). In contrast, pure $ABTS^{+\bullet}$ or DPPH$^\bullet$ are stable during testing period and do not degrade. The scavenging degree is found to be closely dependent on the concentration of Ti_3C_2. A higher concentration of Ti_3C_2 results in more reduction of absorbance, indicating higher removal degree of $ABTS^{+\bullet}$ (Fig. S1†) and DPPH$^\bullet$ (Fig. S2†). This proves that Ti_3C_2 has excellent antioxidant capacity, and its antioxidant mechanism may be related to both electron and proton transfer pathways. Compared the DPPH$^\bullet$ scavenging ability with other antioxidants or nanoparticles (Table S2†), Ti_3C_2 can remove DPPH$^\bullet$ in a smaller dose and shorter time, which indicates that Ti_3C_2 has strong free radical scavenging ability and fast response.[48–51]

Considering ROS play the critical role in regulation of oxidative stress balance, three representative ROS in biological conditions, H_2O_2, $^\bullet$OH and $O_2^{-\bullet}$, were selected to investigate systematically the powerful ROS scavenging capabilities of Ti_3C_2. The ability of Ti_3C_2 to reduce H_2O_2 is evaluated by using HRP–H_2O_2–TMB system, which is a classic enzymatic reaction. Under catalysis of HRP, TMB can be quickly oxidized by H_2O_2 to

produce typical blue color and characteristic absorption. However, when Ti_3C_2 was interacted with H_2O_2, the TMB oxidation degree decreased evidently as reflected by the reduction of characteristic absorption at 652 nm. This indicates that Ti_3C_2 can reduce H_2O_2 thus inhibit the oxidation of TMB. The H_2O_2 reduction activity also shows concentration dependence on the concentration of Ti_3C_2. Higher amount of Ti_3C_2 is used to react with H_2O_2, the oxidation of TMB is inhibited to a higher degree (Fig. 2c). In the interaction with nanomaterials, it is well recognized that the reduction of H_2O_2 may go through 2 pathways, (1) disproportionation reaction produces O_2 and H_2O, and (2) reduction reaction produces water. We used dissolved oxygen meter and ESR oximetry to detect whether the oxygen is produced from the mixture of H_2O_2 and Ti_3C_2, but no signal from oxygen production was detected. This indicates Ti_3C_2 NSs have high chemically reducing ability to H_2O_2.

The antioxidant potential of Ti_3C_2 to clear $^{\bullet}OH$ and $O_2^{\bullet-}$ was evaluated by ESR. Typically, the $^{\bullet}OH$ was generated by the Fenton reaction in Fe^{2+}–H_2O_2 system. The DMPO, was used to capture $^{\bullet}OH$ and form DMPO/$^{\bullet}OH$ spin adduct which shows characteristic ESR peaks with intensity of 1 : 2 : 2 : 1. Compared with control without Ti_3C_2, the addition of 0.1 mg mL^{-1} Ti_3C_2 results in more than 90% reduction of signal intensity, 0.2 mg mL^{-1} Ti_3C_2 can completely scavenge the $^{\bullet}OH$ signal (Fig. 2d). This result verifies that Ti_3C_2 NSs have strong $^{\bullet}OH$ scavenging ability. It is noteworthy that the signal intensity of DMPO/$^{\bullet}OH$ increased considerably at the dosage of 0.05 mg mL^{-1}, which seems like contrary to the antioxidant capability of Ti_3C_2. This is due to that Ti_3C_2 can reduce Fe^{3+} to Fe^{2+} thus accelerate Fenton reaction to produce more hydroxyl radicals. The hydroxyl radical generating system by light irradiating TiO_2 NPs was further employed to confirm the hydroxyl radical scavenging ability of Ti_3C_2 in a concentration dependent manner (Fig. S3†).

To evaluate the $O_2^{\bullet-}$ scavenging activity of Ti_3C_2, the $O_2^{\bullet-}$ was generated by an enzymatic xanthine/XOD system. BMPO is used as a typical spin trap for superoxide. Addition of XOD to the solution containing xanthine, DTPA, and BMPO in pH = 7.4 PBS buffer produces a strong ESR signal with peak intensity of 1 : 1 : 1 : 1 attributable to BMPO/$^{\bullet}OOH$ (Fig. 2e). The ESR signal intensity decreases greatly when Ti_3C_2 was added, suggestive of its antioxidant ability to scavenge superoxide. The scavenging activity is highly dependent on the concentration of Ti_3C_2. In comparison, 0.1 mg mL^{-1} Ti_3C_2 NSs can scavenge almost all the superoxide produced, indicating their excellent superoxide scavenging activity.

In order to prove the broad-spectrum antioxidant ability to scavenge free radicals, $^{\bullet}NO$ as a representative RNS was used to investigate RNS elimination capabilities of Ti_3C_2. SNAP and PTIO$^{\bullet}$ were chosen as the $^{\bullet}NO$ donor and label molecule, respectively. PTIO$^{\bullet}$ is stable oxygen center free radicals, which has typical five-line ESR spectrum with relative intensity of 1 : 2 : 3 : 2 : 1. PTIO$^{\bullet}$ is also a common $^{\bullet}NO$ scavenger, which can react with $^{\bullet}NO$ to yield PTI, resulting in the reduction of the five-line spectrum and generation of seven-line spectrum. The addition of Ti_3C_2 NSs into the mixture of PTIO$^{\bullet}$ and SNAP significantly inhibits the formation of PTI under pH 7.4 (Fig. 2f), and a dosage of 10 μg mL^{-1} can completely remove the $^{\bullet}NO$ signal, indicating the superior $^{\bullet}NO$ radical scavenging ability of

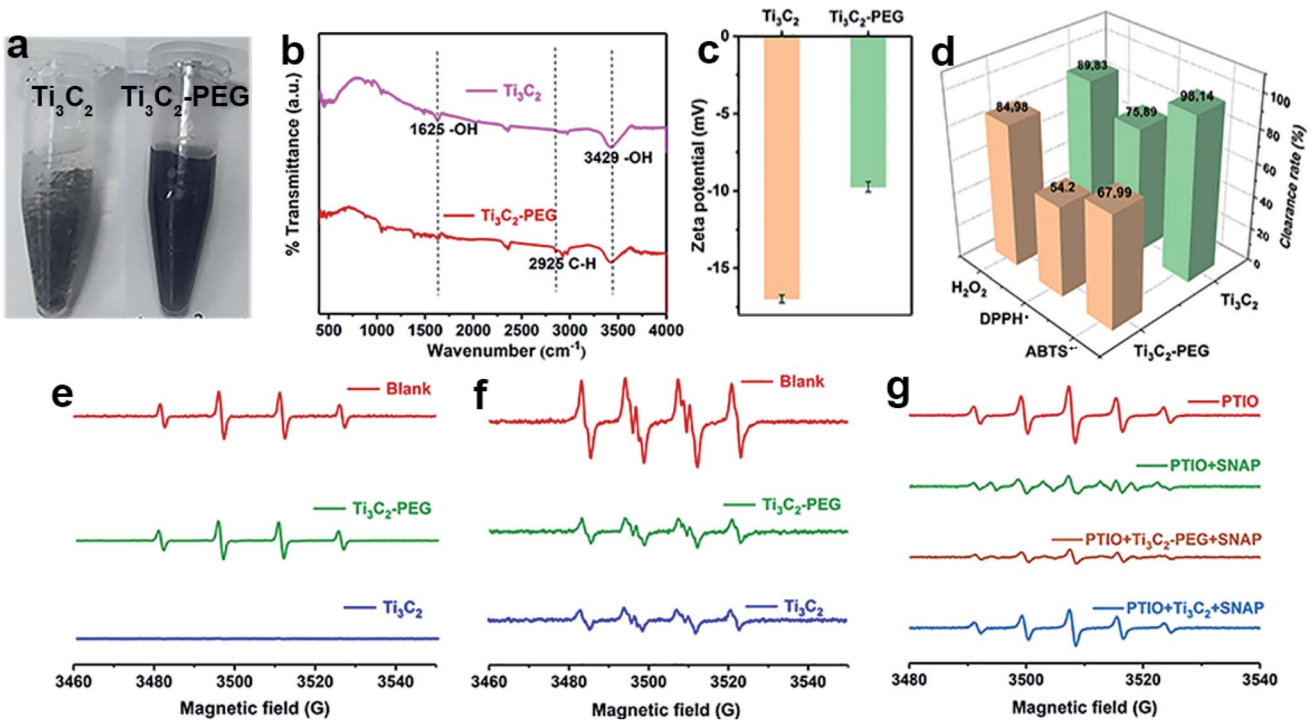

Fig. 3 Stability and antioxidant activity of PEG modified Ti_3C_2 (Ti_3C_2–PEG). (a) Photographs of pristine Ti_3C_2 and Ti_3C_2–PEG suspended in 100 mM pH 7.4 PBS solution, (b) FTIR spectra and (c) zeta potential of Ti_3C_2 and Ti_3C_2–PEG, (d) comparison of Ti_3C_2 and Ti_3C_2–PEG for their scavenging activity toward $ABTS^{+\bullet}$, $DPPH^{\bullet}$ and H_2O_2, the scavenging activity toward (e) $^{\bullet}OH$, (f) $O_2^{\bullet-}$ and (g) $^{\bullet}NO$ of Ti_3C_2 and Ti_3C_2–PEG.

Ti_3C_2 NSs. Interestingly, it is found that the ESR signal of PTIO$^{\bullet}$ also disappeared when more Ti_3C_2 (20 μg mL^{-1}) was added, this indicates that Ti_3C_2 can also scavenge oxygen-centered free radical PTIO$^{\bullet}$ (Fig. S4†).

Compared with natural antioxidant molecules at same dosage, we found that Ti_3C_2 was 2.7 times more potent than TA and 3.3 times more potent than AA in scavenging ABTS$^{+\bullet}$ (Fig. 2g). In addition, Ti_3C_2 is more active than AA and TA in scavenging DPPH$^{\bullet}$ and H_2O_2. Interestingly, AA and TA show weak ability to reduce PTIO$^{\bullet}$ and $^{\bullet}$NO but Ti_3C_2 can scavenge them efficiently, indicating that Ti_3C_2 has a broader range scavenging ability than that of conventional antioxidants. Taken into together, Ti_3C_2 NSs can not only reduce various ROS and RNS (*e.g.* H_2O_2, $^{\bullet}$OH, $O_2^{\bullet-}$, and $^{\bullet}$NO), but also scavenge nitrogen and oxygen-center free radicals, showing more efficient and broad antioxidant capability. The antioxidant capacity is higher than that of natural antioxidants, which is essential for reducing oxidative stress levels to prevent oxidative damage to biological structures.

3.3 Stability and antioxidant activity of Ti_3C_2–PEG NSs

As discussed above, Ti_3C_2 with excellent antioxidant capabilities can be an ideal alternative to natural antioxidants. Unfortunately, the as-prepared Ti_3C_2 NSs are easy to be aggregated in physiochemical environment (*e.g.* PBS buffer), which limit largely the biological application of Ti_3C_2. To overcome this problem, we modify Ti_3C_2 surface with a biocompatible molecule (PEG). Fig. 3a shows clearly that PEG modified Ti_3C_2 (Ti_3C_2–PEG) are well dispersed in 100 mM PBS buffer (pH = 7.4) while Ti_3C_2 NSs are aggregated obviously, demonstrating the successful modification of PEG on Ti_3C_2 and increase of the stability. The Fourier transform infrared spectra of Ti_3C_2–PEG shows a new peak appeared at 2925 cm^{-1}, which corresponds to C–H stretching vibration of PEG molecules (Fig. 3b). The surface potential of Ti_3C_2 and Ti_3C_2–PEG was measured to be ~−17 and −9.7 mV, respectively (Fig. 3c). The loading of electrically neutral PEG molecules reduces the negative charge on Ti_3C_2 surface, thus the zeta potential of Ti_3C_2–PEG is decreased. These data together give the direct evidences for the successful modification on PEG. To understand how the modification of PEG affect the antioxidant performance, we have further comparatively studied the bare Ti_3C_2 and Ti_3C_2–PEG for their ability to scavenge the various free radicals. Fig. 3d–g display the scavenging effect of Ti_3C_2 and Ti_3C_2–PEG at fixed concentration on ABTS$^{+\bullet}$, DPPH$^{\bullet}$, H_2O_2, $^{\bullet}$OH, $O_2^{\bullet-}$ and $^{\bullet}$NO. Behave like Ti_3C_2, Ti_3C_2–PEG shows efficient and broad antioxidant activity toward all the kinds of free radicals. In addition, Ti_3C_2–PEG has a stable scavenging ability of ABTS$^{+\bullet}$ at different pH values (Fig. S5†). As expected, the modification of PEG leads to considerable reduction of the antioxidant activity to varying degree for different free radicals. After PEG modification, the ABTS$^{+\bullet}$ and DPPH$^{\bullet}$ free radical scavenging rates reduced by ~20%, while the superoxide scavenging degree is comparable. The reduction of antioxidant activity of Ti_3C_2 due to PEG

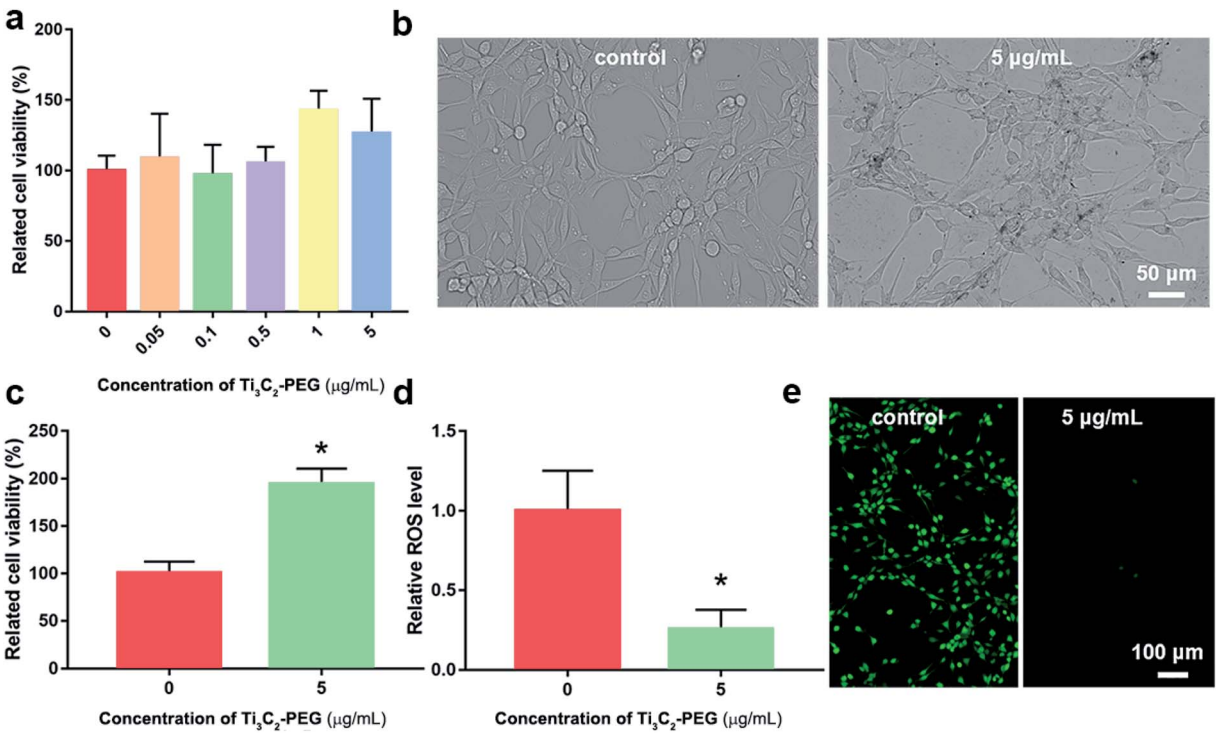

Fig. 4 Protective effect of Ti_3C_2–PEG NSs on NIH3T3 cell. (a) Viability of NIH3T3 cell exposed with different concentration of Ti_3C_2–PEG NSs from CCK-8 assay, (b) images of NIH3T3 cell in cell medium from optical microscope, (c) viability of NIH3T3 cell exposed to 25 μM H_2O_2, (d) the intracellular ROS level of NIH3T3 cell exposed to 25 μM H_2O_2, and (e) fluorescence images of NIH3T3 cell labeled with DCFH-DA; *P < 0.05 compared with the control group.

modification is inevitable, but it is more suitable for stable and biocompatible use in biological applications.

3.4 Cell protection against oxidative damage

In order to investigate the protective role against oxidative stress, the viability and ROS levels of NIH3T3 cell in the absent and present of Ti_3C_2–PEG for 24 h were measured (Fig. 4). Different concentration ranges of Ti_3C_2–PEG NSs were employed firstly to observe their biocompatibility. The cell viability of control group was set as a 100%. As shown in Fig. 4a, Ti_3C_2–PEG NSs did not affect the viability of NIH3T3 cell in the range of testing concentration, indicating their excellent biocompatibility. From the images with optical microscope (Fig. 4b), the dark Ti_3C_2–PEG were observed to exist in the cell medium without changing the morphology of cells, consistent with the good biocompatibility in Fig. 4a. H_2O_2, which was commonly used in inducing oxidative stress, was employed to determine the protective ability of Ti_3C_2–PEG NSs. In the presence of 25 μM H_2O_2, the relative cell viability of NIH3T3 cell increased from 100% to 194% after incubated with 5 μg mL^{-1} Ti_3C_2–PEG NSs (Fig. 4c), and the relative ROS level was also decreased to 1/4 of the control (Fig. 4d). In fluorescence images of DCFH-DA labeled NIH3T3 cells, the ROS level could be observed directly. As shown in Fig. 4e, the green fluorescence almost disappeared after incubated with Ti_3C_2–PEG NSs, which also confirmed that Ti_3C_2–PEG NSs have excellent elimination ability on ROS. These primary results give a promise of antioxidant Ti_3C_2–PEG NSs in cytoprotection and therapy of oxidative stress induced diseases.

3.5 Antioxidant mechanism of Ti_3C_2 NSs

As we known, Ti_3C_2 is easily to be oxidized because of low valence of Ti with unoccupied surface, thus showing excellent reductive potential. For full understanding of the antioxidant mechanism of Ti_3C_2 NSs, it is highly required to know how the changes in the surface and valence structure during oxidation. The Ti_3C_2 NSs sample before and after oxidation by $ABTS^{+\bullet}$ (Ti_3C_2-A) or H_2O_2 (Ti_3C_2-B) were employed for comparative study. After oxidation by $ABTS^{+\bullet}$, TEM shows that small particles appeared on the edge of Ti_3C_2 nanosheets (Fig. 5a). After

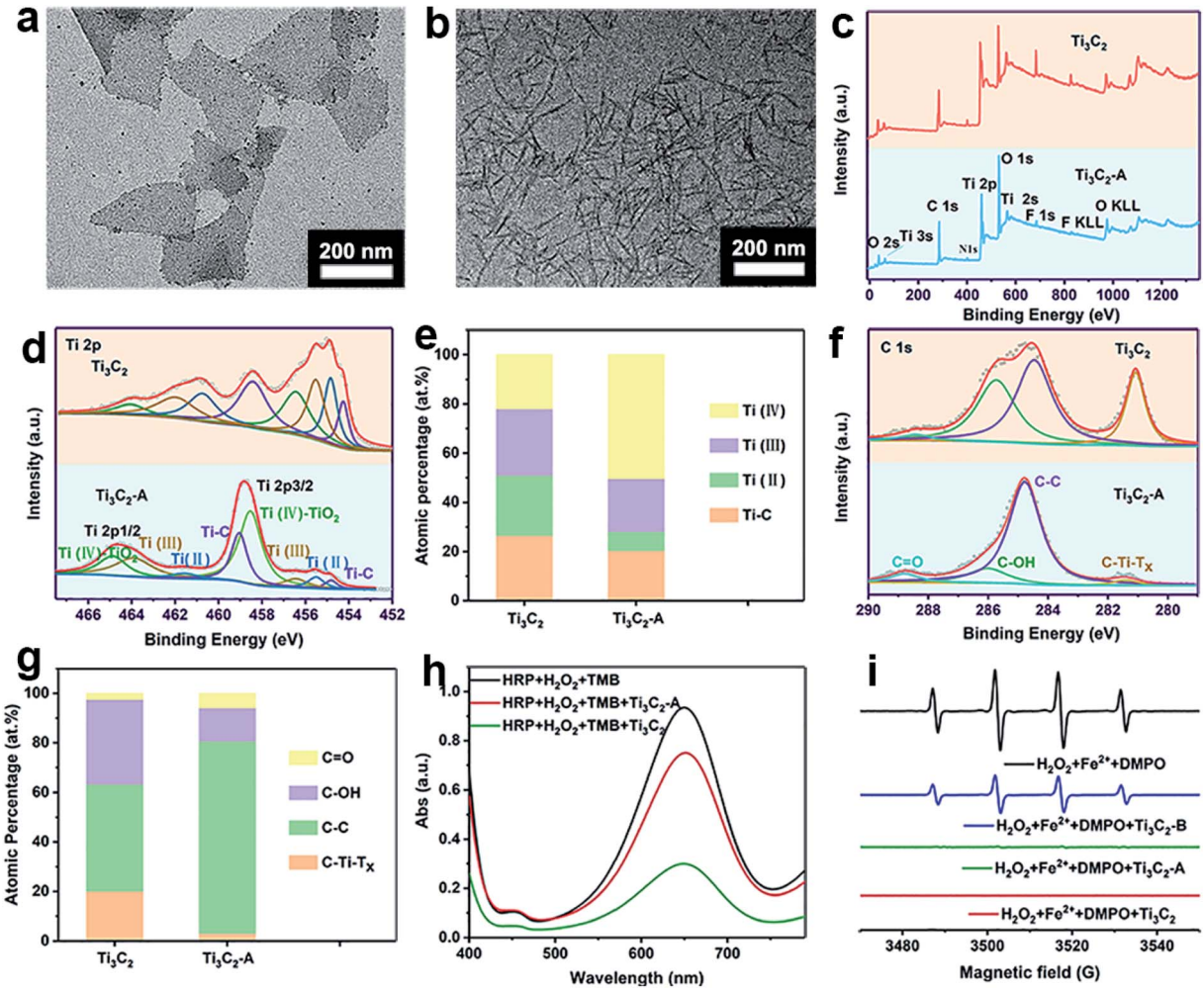

Fig. 5 Antioxidant mechanism of Ti_3C_2 NSs. TEM image of Ti_3C_2-A (a) and Ti_3C_2-B (b), (c) XPS survey spectra, (d) high resolution XPS spectra of Ti 2p, (e) atomic percentages of different Ti species, (f) high resolution XPS spectra of C 1s, (g) atomic percentages of C═O, C–OH, C–C and C–Ti, (h) comparison of H_2O_2 scavenging and (i) $^{\bullet}OH$ scavenging ability of Ti_3C_2, Ti_3C_2-A and Ti_3C_2-B.

scavenging H_2O_2, Ti_3C_2 NSs have a great change in morphology, which seems to be caused by oxidation, leading to further fragmentation of layers (Fig. 5b). It can be seen from the XPS surveys of Ti_3C_2 and Ti_3C_2-A, the relative intensity of O 1s signal was evidently increased, indicating the oxygen participated in the oxidation of Ti_3C_2 during $ABTS^{+\bullet}$ clearance (Fig. 5c). Fig. 5d fitted the XPS spectrum of Ti 2p signal for Ti_3C_2 and Ti_3C_2-A, both of which shows the signal from Ti–C, Ti(II), Ti(III) and Ti(IV),[52,53] but exhibit different ratios. The percentage of Ti–C, Ti(II), Ti(III) and Ti(IV) was calculated to be 26.6%, 24.38%, 27.12%, 21.9% for original Ti_3C_2. In the case of Ti_3C_2-A, the corresponding percentage was 20.42%, 7.86%, 21.37% and 50.35%, respectively (Fig. 5e). Obviously, the proportion of Ti(II) reduced by 3 times while the proportion of Ti(IV) increased by more than 2 times. A slight reduction of the composition of Ti–C and Ti(III) was observed after oxidation. After oxidation with H_2O_2 (Ti_3C_2-B), the signals from Ti–C and Ti(II) disappeared, all the Ti species were converted into Ti(III) and Ti(IV) with percentage of 46.86% and 53.14%, respectively (Fig. S6†). The chemical bonding environment of atomic C was also analyzed by C 1s core level spectra (Fig. 5f and g). C 1s spectrum was fitted into five deconvoluted Gaussian peaks which corresponds to the C–Ti–T_x, C–C, C–OH and C═O, respectively. It clearly shows that the signal intensity of peaks C–OH and C–Ti–T_x decreased greatly after the Ti_3C_2 was oxidized, while the peaks C–C and C–O increased significantly. The ratio of C–Ti–T_x, C–C, C–OH and C═O in Ti_3C_2 before and after oxidation was calculated and compared (Fig. 5g). The significant decrease of C–OH and C–Ti content and the increase of C–C may indicate that part of Ti–C bond was broken after oxidation. The increase of Ti–O and the decrease of Ti–O–H in O 1s spectra also verify the oxidation process of Ti_3C_2 and the reduction of surface OH groups (Fig. S7†). The XRD patterns indicate the obvious change in crystal structure of Ti_3C_2 after oxidation with either $ABTS^{+\bullet}$ or H_2O_2 (Fig. S8†). Especially, the diffraction peaks characteristic to anatase in Ti_3C_2-B reflect the formation of TiO_2 particles. These results prove not only the oxidation reaction occurring between Ti_3C_2 and oxidative species, but also the structure change after oxidation (Fig. S9†).

The gradual transformation of Ti_3C_2 nanosheets during oxidation may endow them intrinsic antioxidant capability. Thus, we test whether the Ti_3C_2 nanosheets after scavenging $ABTS^{+\bullet}$ can scavenge ROS. We collected Ti_3C_2 (Ti_3C_2-A) after complete oxidation with $ABTS^{+\bullet}$, and found that the Ti_3C_2-A cannot reduce $ABTS^{+\bullet}$ but still can further eliminate H_2O_2 and hydroxyl radical. Compared with pristine Ti_3C_2, Ti_3C_2-A exhibit significantly decreased but considerable activity to reduce H_2O_2 (Fig. 5h). However, it exhibits almost unreduced ability to scavenge hydroxyl radicals (Fig. 5i). The Ti_3C_2 nanosheets after oxidation by H_2O_2 (Ti_3C_2-B), also show evident activity to reduce hydroxyl radicals but decreased considerably. This result indicate that the Ti_3C_2 undergoes a gradient oxidation process when interact with oxidizing substances with distinct redox potential. The gradient oxidation event may be related to the abundant and mixed-valence Ti species in Ti_3C_2. When it reduces an oxidant, it still has the ability to remove free radicals with stronger oxidizing power. Scheme 1 illustrates the possible mechanism for gradient oxidation of Ti_3C_2 and the corresponding changes in morphology, chemical valences and antioxidant ability to scavenge ROS, RNS and free radicals. Based on comprehensive analysis, it can be hypothesized that the antioxidant behavior of Ti_3C_2 NSs is different from that of small

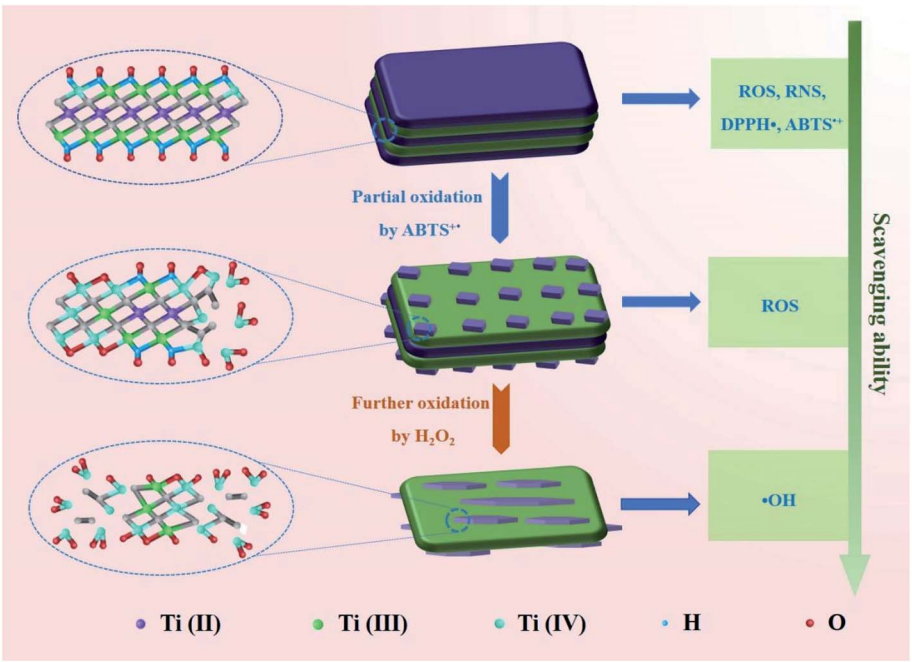

Scheme 1 Schematic diagram illustrating the mechanism for gradient oxidation of Ti_3C_2 MXene and the corresponding changes in scavenging ability of ROS, RNS and free radicals.

molecules and enzymes, but it reflects the characteristics of both. Firstly, because of the Ti species with low valences (Ti^{2+} and Ti^{3+}), Ti_3C_2 NSs show very low redox potential and high reducing ability like natural antioxidant molecules. Secondly, the electron-rich quasi-metallic property induced strong electron transfer ability makes Ti_3C_2 behave like antioxidant nanozymes that can scavenge free radicals. At last, the gradient oxidation behavior accounts for superior and controllable antioxidant capability.

4. Conclusions

The efficient and broad-spectrum antioxidant capability of 2D Ti_3C_2 MXene nanosheets have been demonstrated systematically toward scavenging ROS (H_2O_2, $^{\bullet}OH$, $O_2^{\bullet-}$), RNS ($^{\bullet}NO$) and free radicals ($ABTS^{+\bullet}$, $DPPH^{\bullet}$ and $PTIO^{\bullet}$). Regardless of the antioxidant activity or the types of free radicals that can be scavenged, Ti_3C_2 nanosheets are more powerful than natural antioxidants (AA and TA). The Ti species with unsaturated valence state and the quasi-metallic property induced superior electron transfer ability endow Ti_3C_2 NSs with efficient antioxidant activity. Benefiting from this superior antioxidant performance, we demonstrated *in vitro* that PEG modified Ti_3C_2 with good biocompatibility and stability can effectively protect the normal cells against oxidative stress induced damages. The antioxidant mechanism based on the gradient oxidation of Ti_3C_2 in interaction with oxidative species was revealed. This work demonstrates the application of antioxidant Ti_3C_2 in prevention of ROS induced cell damage, exploring other MXenes with excellent antioxidant capacity and their potential applications in biological protection and treatment of oxidative stress related diseases will be the future direction.

Conflicts of interest

The authors declare no competing financial interests.

Acknowledgements

This work is supported financially by the Program for Zhongyuan Leading Talents of Science and Technology Innovation in Henan Province (204200510016) and the National Natural Science Foundation of China (51772256).

References

1 L. Ilaria, R. Gennaro, C. Francesco, B. Giulia, A. Luisa, D. M. David, G. Gaetano, T. Gianluca, C. Francesco, B. Domenico and A. Pasquale, *Clin. Interventions Aging*, 2018, **13**, 757–772.
2 B. Halliwell, *Annu. Rev. Nutr.*, 1996, **16**, 33–50.
3 B. Uttara, A. V. Singh, P. Zamboni and R. T. Mahajan, *Curr. Neuropharmacol.*, 2009, **7**, 65–74.
4 A. Igor, *Oxid. Med. Cell. Longevity*, 2011, **5**, 293769.
5 W. Ding, L. G. Hudson and K. Liu, *Mol. Cell. Biochem.*, 2005, **279**, 105–112.
6 S. Li, H. Tan, N. Wang, Z. Zhang, L. Lao, C. Wong and Y. Feng, *Int. J. Mol. Sci.*, 2015, **16**, 26087–26124.
7 S. Percário, A. D. Barbosa, E. L. Varela, A. R. Gomes, M. E. Ferreira, T. D. Moreira and M. F. Dolabela, *Oxid. Med. Cell. Longevity*, 2020, **2020**, 1–23.
8 X. Lei, J. Zhu, W. Cheng, Y. Bao, Y. Ho, A. R. Reddi, A. Holmgren and E. S. Arnér, *Physiol. Rev.*, 2016, **96**, 307–364.
9 J. Wu, X. Wang, Q. Wang, Z. Lou, S. Li, Y. Zhu, L. Qin and H. Wei, *Chem. Soc. Rev.*, 2019, **48**, 1004–1076.
10 D. Jiang, D. Ni, Z. T. Rosenkrans, P. Huang, X. Yan and W. Cai, *Chem. Soc. Rev.*, 2019, **48**, 3683–3704.
11 Y. Huang, J. Ren and X. Qu, *Chem. Rev.*, 2019, **119**, 4357–4412.
12 H. Wei, L. Gao, K. Fan, J. Liu, J. He, X. Qu, S. Dong, E. Wang and X. Yan, *Nano Today*, 2021, **40**, 101269.
13 H. Dong, C. Zhang, Y. Fan, W. Zhang, N. Gu and Y. Zhang, *Prog. Biochem. Biophys.*, 2018, **45**, 105–117.
14 B. Yang, Y. Chen and J. Shi, *Chem. Rev.*, 2019, **119**, 4881–4985.
15 Y. Liu, Y. Mao, E. Xu, H. Jia, S. Zhang, V. L. Dawson, T. M. Dawson, Y. Li, Z. Zheng and W. He, *Nano Today*, 2021, **36**, 101027.
16 X. Mu, H. He, J. Wang, W. Long, Q. Li, H. Liu, Y. Gao, L. Yang, Q. Ren, S. Sun, J. Wang, J. Yang, Q. Liu, Y. Sun, C. Liu, X. Zhang and W. Hu, *Nano Lett.*, 2019, **19**, 4527–4534.
17 S. Onizawa, K. Aoshiba, M. Kajita, Y. Miyamoto and A. Nagai, *Pulm. Pharmacol. Ther.*, 2009, **22**, 340–349.
18 R. Zhang, L. Chen, Q. Liang, J. Xi, H. Zhao, Y. Jin, X. Gao, X. Yan, L. Gao and K. Fan, *Nano Today*, 2021, **41**, 101317.
19 G. Tang, J. He, J. Liu, X. Yan and K. Fan, *Exploration*, 2021, **1**, 75–89.
20 G. R. Navale, C. S. Rout, K. N. Gohil, M. S. Dharne, D. J. Late and S. S. Shinde, *RSC Adv.*, 2015, **5**, 74726–74733.
21 C. Liu, Y. Yan, X. Zhang, Y. Mao, X. Ren, C. Hu, W. He and J. Yin, *Nanoscale*, 2020, **12**, 3068–3075.
22 N. Singh, M. A. Savanur, S. Srivastava, P. D'Silva and G. Mugesh, *Angew. Chem., Int. Ed.*, 2017, **56**, 14267–14271.
23 W. Zhang, S. Hu, J. Yin, W. He, W. Lu, M. Ma, N. Gu and Y. Zhang, *J. Am. Chem. Soc.*, 2016, **138**, 5860–5865.
24 J. Dong, L. Song, J. Yin, W. He, Y. Wu, N. Gu and Y. Zhang, *ACS Appl. Mater. Interfaces*, 2014, **6**, 1959–1970.
25 Y. Mao, F. Jia, T. Jing, T. Li, H. Jia and W. He, *ACS Biomater. Sci. Eng.*, 2021, **9**, 569–579.
26 M. Naguib, M. Kurtoglu, V. Presser, J. Lu, J. Niu, M. Heon, L. Hultman, Y. Gogotsi and M. W. Barsoum, *Adv. Mater.*, 2011, **23**, 4248–4253.
27 M. R. Lukatskaya, O. Mashtalir, C. Ren, Y. Dall'Agnese, P. Rozier, P. L. Taberna, M. Naguib, P. Simon, M. W. Barsoum and Y. Gogotsi, *Science*, 2013, **341**, 1502–1505.
28 A. V. Mohammadi, J. Rosen and Y. Gogotsi, *Science*, 2021, **372**, 1165.
29 Q. Lu, J. Wang, B. Li, C. Weng, X. Li, W. Yang, X. Yan, J. Hong, W. Zhu and X. Zhou, *Anal. Chem.*, 2020, **92**, 7770–7777.
30 Z. Zeng, Y. Yan, J. Chen, P. Zan, Q. Tian and P. Chen, *Adv. Funct. Mater.*, 2019, **29**, 1806500.

31 S. Iravani and R. S. Varma, *ACS Biomater. Sci. Eng.*, 2021, **7**, 1900–1913.
32 R. Liang, Y. Li, M. Huo, H. Lin and Y. Chen, *ACS Appl. Mater. Interfaces*, 2019, **11**, 42917–42931.
33 J. Li, Z. Li, X. Liu, C. Li, Y. Zheng, K. W. Yeung, Z. Cui, Y. Liang, S. Zhu and W. Hu, *Nat. Commun.*, 2021, **12**, 1224.
34 X. Zhao, A. Vashisth, E. Prehn, W. Sun, S. A. Shah, T. Habib, Y. Chen, Z. Tan, J. L. Lutkenhaus, M. Radovic and M. J. Green, *Matter*, 2019, **1**, 513–526.
35 W. Feng, X. Han, H. Hu, M. Chang, L. Ding, H. Xiang, Y. Chen and Y. Li, *Nat. Commun.*, 2021, **12**, 2203.
36 X. Zhao, L. Wang, J. Li, L. Peng, C. Tang, X. Zha, K. Ke, M. Yang, B. Su and W. Yang, *Adv. Sci.*, 2021, **8**, e2101498.
37 J. Liu, W. Lu, X. Lu, L. Zhang, H. Dong and Y. Li, *Nano Res.*, 2021, 1–9.
38 X. Ren, M. Huo, M. Wang, H. Lin, X. Zhang, J. Yin, Y. Chen and H. Chen, *ACS Nano*, 2019, **13**, 6438–6454.
39 Z. Qi, S. Wang, Y. Li, L. Wang, L. Zhao, Q. Ge and J. Zhang, *Ceram. Int.*, 2021, **47**, 16555–16561.
40 L. Wang, N. Zhang, Y. Li, W. Kong, J. Gou, Y. Zhang, L. Wang, G. Yu, P. Zhang, H. Cheng and L. Qu, *ACS Appl. Mater. Interfaces*, 2021, **13**, 42442–42450.
41 F. Han, S. Luo, L. Xie, J. Zhu, W. Wei, X. Chen, F. Liu, W. Chen, J. Zhao and L. Dong, *ACS Appl. Mater. Interfaces*, 2019, **11**, 8443–8452.
42 M. Alhabeb, K. Maleski, B. Anasori, P. Lelyukh, L. Clark, S. Sin and Y. Gogotsi, *Chem. Mater.*, 2017, **29**, 7633–7644.
43 T. S. Mathis, K. Maleski, A. Goad, A. Sarycheva, M. Anayee, A. C. Foucher, K. Hantanasirisakul, C. E. Shuck, E. A. Stach and Y. Gogotsi, *ACS Nano*, 2021, **15**, 6420–6429.
44 C. Cao, E. Kim, Y. Liu, M. Kang, J. Li, J. Yin, H. Liu, X. Qu, C. Liu, W. E. Bentley and G. F. Payne, *Biomacromolecules*, 2018, **19**, 3502–3514.
45 S. Z. Khan, Z. Rehman, I. S. Butler and F. Bélanger-Gariepy, *Inorg. Chem. Commun.*, 2019, **105**, 140–146.
46 R. Re, N. Pellegrini, A. Proteggente, A. Pannala, M. Yang and C. Rice-Evans, *Free Radical Biol. Med.*, 1999, **26**, 1231–1237.
47 P. Goupy, A. B. Bautista-Ortin, H. Fulcrand and O. Dangles, *J. Agric. Food Chem.*, 2009, **57**, 5762–5770.
48 S. Z. Khan, Z. Khan, I. Ahmad, S. Khan, S. Khan, M. Ahmed, M. Inam, F. Belanger-Gariepy and Z. U. Rehman, *Inorg. Chem. Commun.*, 2021, **123**, 108316.
49 I. Ahmad, Z. U. Rehman, A. Waseem, M. Tariq, C. MacBeth, J. Bacsa, D. Venkataraman, A. Rajakumar, N. Ullah and S. Tabassum, *Inorg. Chim. Acta*, 2020, **505**, 119433.
50 Q. Li, M. Duan, L. Liu, X. Chen, Y. Fu, J. Li, T. Zhao and D. J. McClements, *J. Agric. Food Chem.*, 2021, **69**, 9661–9670.
51 N. Ajmal, K. Saraswat, M. A. Bakht, Y. Riadi, M. J. Ahsan and M. Noushad, *Green Chem. Lett. Rev.*, 2019, **12**, 244–254.
52 R. Li, X. Ma, J. Li, J. Cao, H. Gao, T. Li, X. Zhang, L. Wang, Q. Zhang, G. Wang, C. Hou, Y. Li, T. Palacios, Y. Lin, H. Wang and X. Ling, *Nat. Commun.*, 2021, **12**, 1587.
53 X. Zhao, A. Vashisth, E. Prehn, W. Sun, S. A. Shah, T. Habib, Y. Chen, Z. Tan, J. L. Lutkenhaus, M. Radovic and M. J. Green, *Matter*, 2019, **1**, 513–526.